

# Graphene–Metal–Organic Framework Composite Sulfur Electrodes for Li–S Batteries with High Volumetric Capacity

Avery E. Baumann,<sup>#</sup> Julia R. Downing,<sup>#</sup> David A. Burns, Mark C. Hersam,<sup>\*</sup> and V. Sara Thoi<sup>\*</sup>Cite This: *ACS Appl. Mater. Interfaces* 2020, 12, 37173–37181

Read Online

ACCESS |



Metrics &amp; More



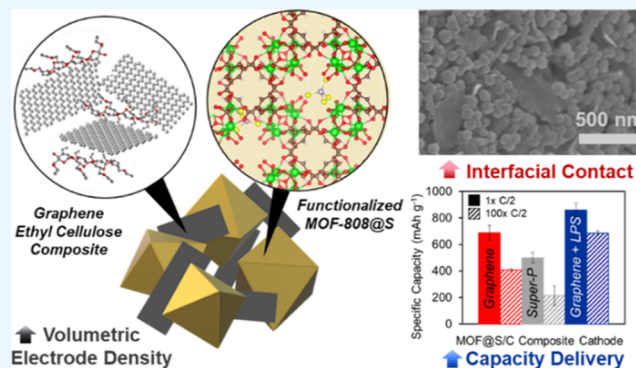
Article Recommendations



Supporting Information

**ABSTRACT:** In an age of rapid acceleration toward next-generation energy storage technologies, lithium–sulfur (Li–S) batteries offer the desirable combination of low weight and high specific energy. Metal–organic frameworks (MOFs) have been recently studied as functionalizable platforms to improve Li–S battery performance. However, many MOF-enabled Li–S technologies are hindered by low capacity retention and poor long-term performance due to low electronic conductivity. In this work, we combine the advantages of a Zr-based MOF-808 loaded with sulfur as the active material with a graphene/ethyl cellulose additive, leading to a high-density nanocomposite electrode requiring minimal carbon. Our electrochemical results indicate that the nanocomposites deliver enhanced specific capacity over conventionally used carbon/binder mixtures, and postsynthetic modification of the MOF with lithium thiophosphate results in further improvement. Furthermore, the dense form factor of the sulfur-loaded MOF–graphene nanocomposite electrodes provides high volumetric capacity compared to other works with significantly more carbon additives. Overall, we have demonstrated a proof-of-concept paradigm where graphene nanosheets facilitate improved charge transport because of enhanced interfacial contact with the active material. This materials engineering approach can likely be extended to other MOF systems, contributing to an emerging class of two-dimensional nanomaterial-enabled Li–S batteries.

**KEYWORDS:** lithium–sulfur battery, metal–organic framework, graphene, nanocomposite, high packing density, energy storage, volumetric capacity, thiophosphate



## INTRODUCTION

Societal demands for lighter, more sustainable, and higher-performing energy storage devices necessitate the development of post-lithium-ion battery technologies. A strong candidate has emerged in lithium–sulfur (Li–S) batteries as result of the high theoretical energy density (2600 W h kg<sup>-1</sup> and 2800 W h L<sup>-1</sup>) and low cost of sulfur.<sup>1</sup> However, Li–S batteries face key issues including severe capacity loss due to polysulfide dissolution and low electrode conductivity, which limit performance and prevent wide-scale adoption of the technology.<sup>2</sup> In addition, low sulfur conductivity results in poor utilization, which can be partly mitigated by the inclusion of conductive additives to the cathode architecture such as carbonaceous, inorganic, or polymeric materials.<sup>3–8</sup> For efficient electron transfer, these additives must exhibit good interfacial contact with sulfur and the electrolyte to enable efficient battery cycling. The development of conductive materials with suitable morphologies and the ability to sequester sulfur could dramatically improve such interfaces within the electrode and have a significant impact on energy storage capabilities.

We and others have previously demonstrated that metal–organic frameworks (MOFs) are capable of mitigating capacity fade and improving sulfur utilization by retaining sulfur species within the electrode architecture.<sup>9–14</sup> However, MOFs also have several drawbacks that restrict their use in batteries including their electronically insulating nature and low density. Employing sulfur-loaded MOFs (denoted as “@S”), in which the pore space is packed with sulfur, rather than MOFs physically mixed with sulfur (denoted as “+S”), improves volumetric density but limits electrochemical access to sulfur.

Previously reported approaches address this problem by increasing the ratio of conductive carbon nanotubes,<sup>15–18</sup> graphene oxide,<sup>19–22</sup> or polymer<sup>6,23</sup> additives to the sulfur-loaded MOF composite electrode, limiting the utilizable mass of the active material. Others have reduced the MOF particle

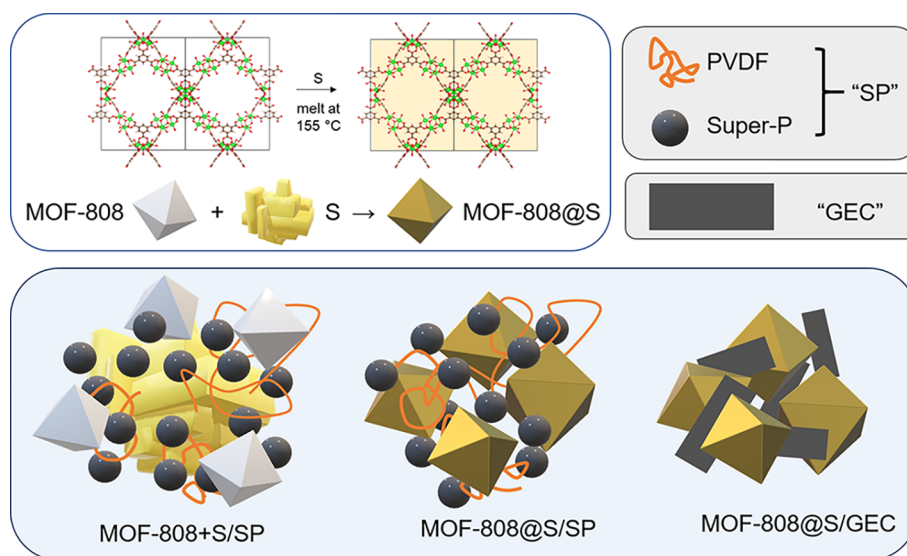
Received: May 27, 2020

Accepted: July 22, 2020

Published: August 5, 2020



**Scheme 1. Illustration of Sulfur Loading Procedure in Representative MOF-808 (Top) and Cartoon Representations of Different Electrode Compositions Highlighting the Volumetric Density Afforded by the Various Components (Bottom)**



size to maximize interparticle contact, but this strategy can also exacerbate polysulfide leaching in MOFs with poor host–guest interactions with sulfur.<sup>9,12,13,24,25</sup> Herein, we offer a unique approach to improve both electrode conductivity and sulfur utilization by using a graphene/ethyl cellulose (GEC) nanocomposite additive.

MOF-808 was selected for this study as a representative MOF to demonstrate the efficacy of our composite strategy because it is easily synthesized and highly porous and features a large number of functionalizable sites on its coordinatively unsaturated Zr metal node.<sup>26</sup> The framework itself is electronically insulating and does not have any electrochemical features that compete with Li–S cycling. The morphologies of sulfur-loaded MOFs and graphene nanoflakes afford cathode slurries with more compact volumes than conventional sulfur-mixed MOF formulations (Scheme 1). These sulfur-loaded MOF and graphene nanoflake composites, denoted as “MOF-808@S/GEC”, present a promising opportunity to utilize versatile MOF chemistries in devices without sacrificing volumetric performance.

In conventional Li–S cathode slurry formulations, an additive weight of 20–30% conductive carbon and polymer binder is needed for sufficient electrical conductivity and slurry adhesion to the current collector, restricting the amount of active material that can be loaded into each electrode.<sup>2,27,28</sup> Utilizing a more conductive carbon material with enhanced interfacial contact has the potential to decrease the mass ratio of carbon to active material. Graphene has historically garnered attention in the field of nanotechnology<sup>29</sup> for its high conductivity,<sup>30</sup> flexibility,<sup>31</sup> and mass producibility.<sup>32</sup> These properties make graphene a strong candidate to replace conventional, amorphous carbon black (Super-P) as a conductive material in battery construction. Meanwhile, ethyl cellulose, a benign polymer additive commonly used in food production, has been identified as an effective stabilizer for top-down graphene synthesis via liquid phase exfoliation.<sup>33</sup> The result of this synthetic approach is a GEC nanocomposite powder that can be readily redispersed in a variety of solvents, enabling functional inks and coatings.

In previous work, we have demonstrated favorable performance of GEC nanocomposites in cobalt-free lithium ion battery cathodes.<sup>34,35</sup> In these cases, the graphene nanosheets improve charge transport because of their increased conductivity compared to incumbent conductive additives, while ethyl cellulose promotes conformal interfaces between graphene and cathode particles, leading to high volumetric capacity. These results motivated the exploration of GEC in a Li–S battery system, particularly utilizing MOFs as a unique host material for sulfur. Additionally, process innovations were implemented in the graphene synthesis for this work to facilitate scalable production of GEC materials with high graphene loading, making this approach broadly applicable to future studies.

## RESULTS AND DISCUSSION

MOF-808 samples were prepared solvothermally (described in the Supporting Information), activated to remove residual solvent, and subsequently loaded with sulfur by a melt diffusion process at 155 °C to form MOF-808@S (Scheme 1). Sulfur content in the prepared MOF-808@S samples was determined using thermogravimetric analysis (TGA), wherein sulfur is eliminated at temperatures <350 °C. In samples with initial mass loading ratios of 1:1 or 3:2 S/MOF by mass, we achieve sulfur loadings of 57 and 74%, respectively. While the characteristic features of the MOF remain unchanged (Figures S2 and S3), it is worth noting that we also observe evidence of unloaded sulfur in both the TGA and X-ray diffraction pattern in the sample with 74% sulfur loading (“MOF-808@S-high”, Figures S1 and S2), likely because of excess sulfur on the external MOF surface. Qualitative energy-dispersive spectroscopy (EDS) was used to evaluate sulfur uptake into individual MOF crystals (Figure S4). Uniform distribution of the oxygen K $\alpha$ 1 and zirconium L $\alpha$ 1 signal is observed, complying with the expected chemical composition of MOF-808. Additionally, concentrated sulfur penetration into the particle is detected and demonstrates successful volumetric uptake of sulfur in the MOF-808@S particles. These characterization results are in agreement with other reports of sulfur-loaded MOFs.<sup>14–23</sup>

Previously, we explored a functionalized MOF-808 with node-bound lithium thiophosphate (“LPS”) guest molecules.<sup>10</sup>

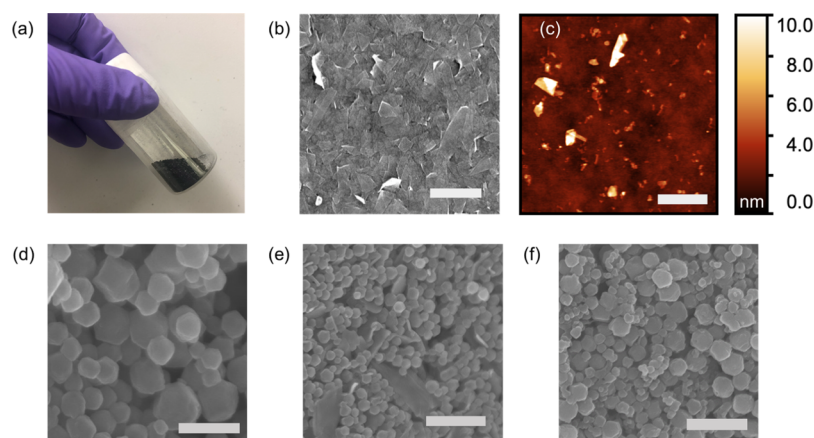


**Figure 1.** (a) Vial containing GEC powder used to prepare cathode slurries. (b) SEM of spin-coated graphene film prepared using material from (a) after thermal pyrolysis of ethyl cellulose. (c) AFM of individual drop-casted graphene flakes from (a) after thermal pyrolysis of ethyl cellulose; average of square root of the flake area is 138.7 nm, with an average maximum flake thickness of 4.02 nm. SEM images of composite samples containing (d) MOF-808@S with 57% S and dried slurries of (e) MOF-808@S/GEC, (f) MOF-808+S/SP-75. Graphene is observed as rectangular flakes in (e), while Super-P particles are visible as smaller spheres in (f). The scale bar represents 1  $\mu\text{m}$  in (b,c), 250 nm in (d), and 500 nm in (e,f).

The thiophosphate moiety improves sulfur utilization and Li–S cyclability through the reversible formation of S–S bonds.<sup>36</sup> We expect that loading sulfur within the LPS-MOF-808, rather than just physically mixing LPS-MOF-808 and S, enables greater chemical interaction between the thiophosphate and sulfur species inside the porous framework. Sulfur-loaded LPS-MOF-808 samples were prepared and characterized in an analogous manner to the aforementioned MOF-808@S samples, resulting in samples with 32 and 59% incorporated sulfur species by mass for loading ratios of 1:1 and 3:2 S/MOF, respectively (Figure S1). We attribute the differences in sulfur loading from the MOF-808@S and LPS-MOF-808@S to the incorporated LPS guest molecule, which takes up the pore space that could otherwise be occupied by sulfur. The sample with only 32% sulfur will be referred to as “LPS-MOF-808@S-low.” For further discussion, the MOF-808@S (57% S) and LPS-MOF-808@S (59% S) samples will be directly compared because of their nearly identical mass percent of encapsulated sulfur.

As previously mentioned, the synthesis of the GEC nanocomposite has been reported for other applications, namely, printed electronics<sup>37</sup> and lithium ion batteries.<sup>34,35</sup> However, further optimization of the shear mixing parameters enables us to maximize the relative weight fraction of graphene to ethyl cellulose in the GEC powder to  $\sim 1:1$ , which is essential to minimize the overall slurry mass while maintaining a high amount of the conductive material in the GEC nanocomposite. In brief, top-down exfoliation of bulk graphite was implemented via inline shear mixing with ethyl cellulose in a pilot-scale manufacturing process. After purifying shear-mixed GEC dispersions by centrifugal postprocessing, graphene nanosheets of controlled size and thickness were stabilized with ethyl cellulose in a dry powder (Figure 1a). Scanning electron microscopy (SEM) and atomic force microscopy (AFM) indicate successful synthesis of large, thin few-layer graphene flakes after pyrolytic decomposition of ethyl cellulose (Figure 1b,c). TGA of the GEC sample is shown in Figure S5; this work was carried out using a GEC powder that was 53% graphene and 47% ethyl cellulose by weight ( $\sim 1:1$  graphene to ethyl cellulose ratio). The high surface area of these graphene nanosheets lends itself to high-quality flake-to-flake contacts in a percolating film (Figure 1b). Detailed flake

size distributions from AFM (Figure 1c) are also provided in Figure S6.

Following synthesis and characterization of the various component materials, MOF composite slurries were prepared using GEC as the only additive contributing to the electronic conductivity (via graphene, as a source of carbon) and cathode stability (via ethyl cellulose, eliminating the need for an additional polymer binder). The superior electronic conductivity of the graphene nanoflakes ( $250 \text{ S cm}^{-1}$ )<sup>31</sup> compared to Super-P ( $5\text{--}30 \text{ S cm}^{-1}$ ),<sup>38</sup> a conventionally used carbon black additive, allows lower weight fractions of the graphene additive (10% by mass) compared to Super-P composites (typically 15% by mass) for efficient electron delivery to the sulfur species.<sup>10,39</sup> In addition, the expected enhanced interfacial contact between GEC and sulfur-loaded MOF enables the omission of poly(vinylidene difluoride) (PVDF), a common polymeric binder used in electrode fabrication that is typically 10% of the slurry mass.<sup>27,40</sup>

SEM images of dried slurries clearly show that the MOF-808@S particles and the graphene flakes are in intimate contact and well-distributed throughout the mixture (Figure 1e). In contrast, images of dried slurries composed of Super-P/PVDF (“MOF-808@S/SP-90”) at the same mass loading exhibit tentatively discernible carbon particles ( $\sim 40 \text{ nm}$  spheres)<sup>38</sup> intermittently in contact with the sulfur-loaded MOF particles (Figures S7 and S8). Only when the Super-P/PVDF content is increased to 25% by mass (“MOF-808@S/SP-75”), are the small Super-P particles visibly in contact with MOF-808@S throughout the slurry (Figures 1f, S7, and S8). EDS analysis of the MOF-808@S/GEC composite slurries (Figure S4) also show strong sulfur  $K\alpha 1$  penetration throughout the sample in addition to a consistent distribution of oxygen and zirconium. In future studies, liquid in situ transmission electron microscopy may be particularly useful to even better visualize how sulfur undergoes conversion within the MOF during cycling.<sup>41</sup>

We employed X-ray photoelectron spectroscopy (XPS) to examine the binding energies of constituent chemical species of the prepared electrode slurries. Spectra for C 1s, S 2p, and Zr 3d regions were collected for each sample to gather information about the GEC, sulfur, and MOF components of the slurry (Figure 2). For this study, three samples were

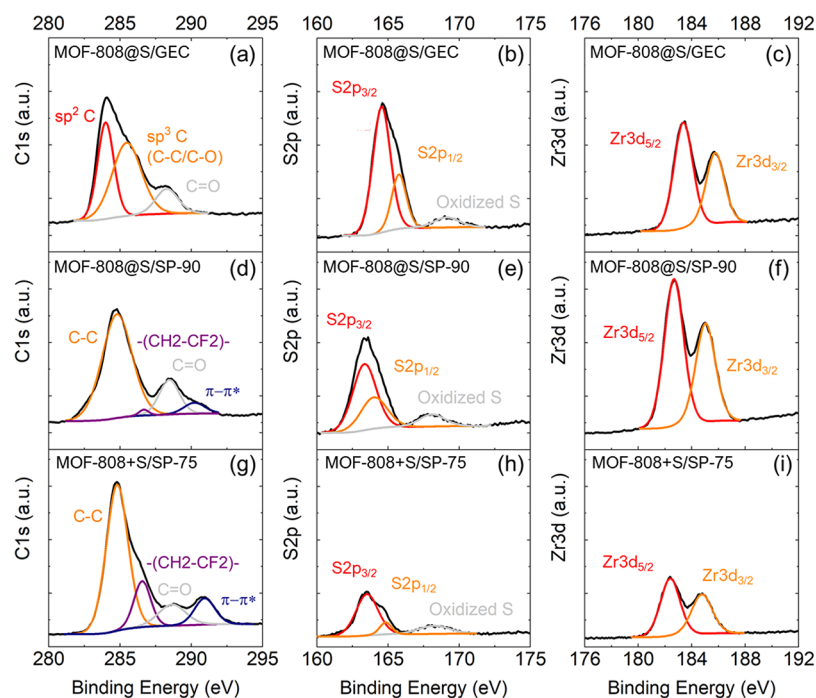


**Figure 2.** Physicochemical analysis of cathode materials via XPS, highlighting differences in C 1s, S 2p, and Zr 3d features for (a–c) MOF-808@S/GEC, (d–f) MOF-808@S/SP-90, and (g–i) MOF-808+S/SP-75 samples. Characteristic  $sp^2$  bonding consistent with graphene is observed for the MOF-808@S/GEC C 1s spectrum, while only  $sp^3$  bonding character is observed for the MOF-808@S/SP-90 and MOF-808+S/SP-75. Evidence of constituent  $CH_2-CF_2$  bonds in the PVDF molecular structure and  $\pi-\pi^*$  delocalization is present in the “SP” C 1s spectra. The S 2p and Zr 3d spectra confirm chemical environments are similar in the MOF-808@S and MOF-808+S samples but differ when mixed with either GEC or Super-P/PVDF to make the slurry composite.

investigated: MOF-808@S/GEC (Figure 2a–c), MOF-808@S/SP-90 (Figure 2d–f), and MOF-808+S/SP (Figure 2g–i). In the C 1s spectra of MOF-808@S/GEC (Figure 2a), constituent  $sp^2$  and  $sp^3$  peaks characteristic of graphene and ethyl cellulose are identified at  $\sim 284$  and  $\sim 285$  eV, respectively, which are qualitatively consistent with our previous report.<sup>42</sup> These C 1s spectra are also in agreement with previously identified features of MOF-808, where the carboxylate feature of the organic linker is also observed.<sup>43,44</sup> The position of the orange peak associated with  $sp^3$  bonding in the GEC sample has a different position than the orange C–C peaks in the C 1s spectra of the slurries prepared with Super-P/PVDF (Figure 2d,g) because of the contribution of C–O bonds in the ethyl cellulose molecular structure in the GEC sample. There are other key differences in the C 1s spectra for the Super-P/PVDF samples; in particular, no  $sp^2$  peak is observed, which is expected for amorphous carbon, while a small peak emerges at  $\sim 286$  eV corresponding to  $-(CH_2-CF_2)-$  monomers in the molecular structure of PVDF.<sup>45</sup> Additionally,  $\pi-\pi^*$  delocalization characteristic of  $CF_2$  in  $-(CH_2-CF_2)-_n$  is distinguishable at  $\sim 291$  eV.<sup>46</sup> Further analysis via Raman spectroscopy (Figure S9) confirms the presence of graphene in the MOF-808@S/GEC specimens.

In the S 2p spectra, for all samples, we observe spin–orbit splitting that yields distinct S  $2p_{1/2}$  and S  $2p_{3/2}$  peaks with the binding energy of the S  $2p_{3/2}$  peaks in the range 163–165 eV and the corresponding S  $2p_{1/2}$  peaks in the range 164–166 eV, which is indicative of an  $S^0$  oxidation state (Figure 2b,e,h). Additionally, a small feature at 168–170 eV is observed in all samples that we attribute to oxidized sulfur. While the S 2p spectra are similar for the three samples, they are not identical. A noticeable peak shift is observed for the S  $2p_{3/2}$  fitted peaks

between the GEC and Super-P/PVDF-containing samples, where the S  $2p_{3/2}$  peak falls at  $\sim 163.5$  eV for the MOF-808@S/SP-90 (Figure 2e) and the MOF-808+S/SP-75 (Figure 2h) samples, but is shifted by almost 1–164.5 eV for the MOF-808@S/GEC sample (Figure 2b). Because the peak positions are consistent for MOF-808@S/SP-90 and MOF-808+S/SP-75, we attribute the observed difference in the MOF-808@S/GEC to the choice of the cathode additive (SP or GEC) and not the sulfur loading procedure.

In all of the Zr 3d spectra, the Zr  $3d_{5/2}$  and Zr  $3d_{3/2}$  peaks are discerned at 182–184 and 184–186 eV, respectively (Figure 2c,f,i), and are in general agreement with previously reported values for MOF-808.<sup>22,44,47</sup> However, it should again be noted that there is noticeable peak shift between the different samples, where the binding energy of the Zr  $3d_{5/2}$  peak is  $\sim 182.5$  eV for the Super-P/PVDF-containing samples (Figure 2f,i), but nearly 1 eV higher (183.4 eV) for the GEC sample (Figure 2c). Consistent with our discussion above, we conclude that the choice of mixing or volumetrically loading sulfur into the MOF has a negligible effect on the positions of the Zr 3d features, while the choice of the carbon source in the slurry (GEC or SP) has a more profound effect. We postulate that the improved interfacial contact between MOF-808@S particles and GEC lead to electrostatic charge shifts, resulting in the positive shifts in the S and Zr electron binding energies and the negative shift in C 1s  $sp^3$  and  $sp^2$  binding energies from reported GEC spectra ( $\sim 1$  eV lower).<sup>42</sup> Further studies using density functional theory (DFT) calculations would be helpful to pinpoint the mechanisms behind these electrostatic charge shifts, drawing upon prior DFT-enabled insights regarding adsorption mechanisms between graphene, sulfur, and long-chain polysulfides.<sup>48</sup>

Armed with physicochemical analyses of our materials indicating successful sulfur uptake within the MOF host and good contact between GEC and sulfur-loaded MOF, we proceeded with electrochemical characterization. Electrodes were prepared by casting the various slurries onto carbon paper supports, as described in the [Supporting Information](#). Galvanostatic cycling experiments were conducted using a charge/discharge rate (“C-rate” where  $1C = 1680 \text{ mA g}^{-1}$ ) of  $C/2$  to evaluate the performance of the different materials and slurry formulations. For cycling discussion, unless otherwise stated, the slurry composition is fixed to 90% MOF-808@S and 10% carbon/binder additives. Additionally, all cathode formulations used in this study are provided in [Table S1](#).

The cells prepared with MOF-808@S/GEC cathodes deliver an average capacity of  $688 \pm 56 \text{ mA h g}^{-1}$  for their first cycle and  $409 \pm 10 \text{ mA h g}^{-1}$  after completing 100 cycles, a significant improvement over cells containing MOF-808@S/SP-90, which delivered an average of  $500 \pm 7$  and  $214 \pm 30 \text{ mA h g}^{-1}$  in the first and 100th cycle, respectively ([Figure 3](#)).

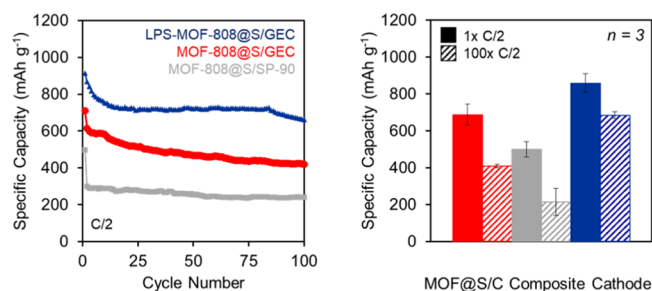


**Figure 3.** (a,b) Representative cycling performance of composite electrodes at a cycling rate of  $C/2$  ( $840 \text{ mA g}^{-1}$ ). LPS-MOF-808@S/GEC cells are better able to utilize sulfur, resulting in higher deliverable capacities than the MOF-808@S/GEC cells. The MOF-808@S/SP-90 cells at the same loading of active material are not able to deliver substantial capacities. Error bars represent one standard deviation.

Only when the SP content is increased to 25% by mass (MOF-808@S/SP-75), are the galvanostatic cycling results comparable to the MOF-808@S/GEC data ([Figure S10](#)), suggesting that the quality of the electronic contact between the carbon and MOF particles is critical. These drastic performance differences highlight the superior ability of GEC to enhance cyclability at low mass loading compared to SP. Furthermore, cathodes constructed with GEC exhibit improved capacity retention compared to those containing Super-P/PVDF—59.4 versus 51.2%, respectively—indicating that GEC is able to mitigate migration of polysulfide species slightly better than Super-P/PVDF ([Figure S10](#)).

Functionalization of MOF-808 showed further enhancement in cycling performance. The LPS-MOF-808@S/GEC cells outperformed their unfunctionalized counterparts with initial and final capacities of  $858 \pm 51$  and  $685 \pm 18 \text{ mA h g}^{-1}$ , respectively, and a capacity retention of 79.8% ([Figure 3](#), triplicate data shown in [Figure S10](#)). The cycling results for LPS-MOF-808@S/GEC cells demonstrate both sulfur utilization and capacity retention are improved compared to the MOF-808@S/GEC cells. We attribute these differences in performance to chemical interaction of the thiophosphate moiety with both sulfur and polysulfides in the cell. Furthermore, the LPS-MOF-808@S/GEC cells deliver capacities that are just slightly diminished from the values of LPS-MOF-808+S/SP-75 (prepared using 75% LPS-MOF-808+S and 25% Super-P + PVDF by mass) achieved in our previous report ( $\sim 1070 \text{ mA h g}^{-1}$ ) in the first cycle at  $C/2$ .<sup>10</sup>

Comparing the MOF-808@S/GEC and MOF-808+S/SP-75 cycling results with and without LPS functionalization, the thiophosphate moiety enhances capacity delivery by 24.7% ( $\sim 170 \text{ mA h g}^{-1}$  out of  $688 \text{ mA h g}^{-1}$ ) in the MOF-808@S cells, whereas the MOF-808+S cells only increase by 11.5% ( $\sim 110 \text{ mA h g}^{-1}$  out of  $960 \text{ mA h g}^{-1}$ ). This capacity enhancement from LPS incorporation is even more drastic in cells prepared with the LPS-MOF-808@S-low/GEC sample (with only 32% by mass sulfur), which yields an average capacity of  $940 \pm 12 \text{ mA h g}^{-1}$ , an increase in capacity of

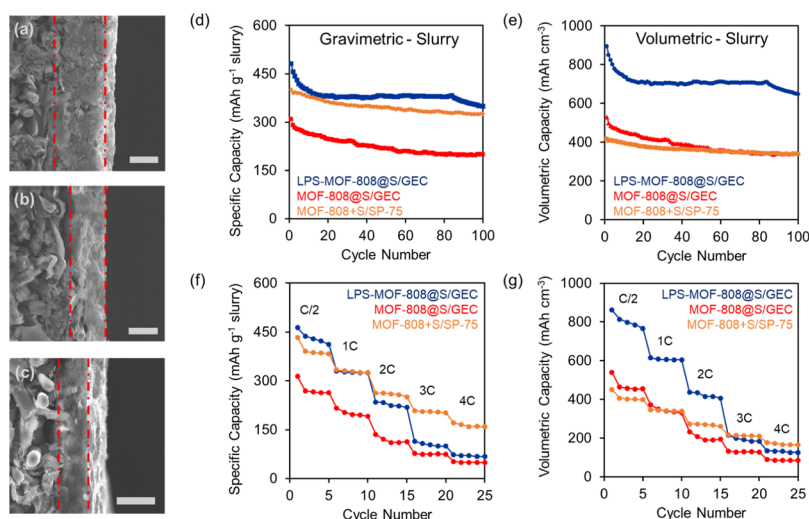


**Figure 4.** Cross-sectional profiles of carbon paper electrodes coated with (a) MOF-808+S/SP-75, (b) MOF-808@S/GEC, and (c) LPS-MOF-808@S/GEC slurries (scale bar is  $20 \mu\text{m}$ ). Comparisons of (d) gravimetric and (e) volumetric capacity based on the slurry highlighting the denser form factor of the MOF-808@S/GEC compared to MOF-808+S/SP-75 composite electrodes. Rate capability performances from  $C/2$  to  $4C$  expressed (f) gravimetrically based on slurry mass and (g) volumetrically based on the slurry thickness. The sulfur-loaded MOF cells suffer at rates above  $2C$  because of mass transport limitations.

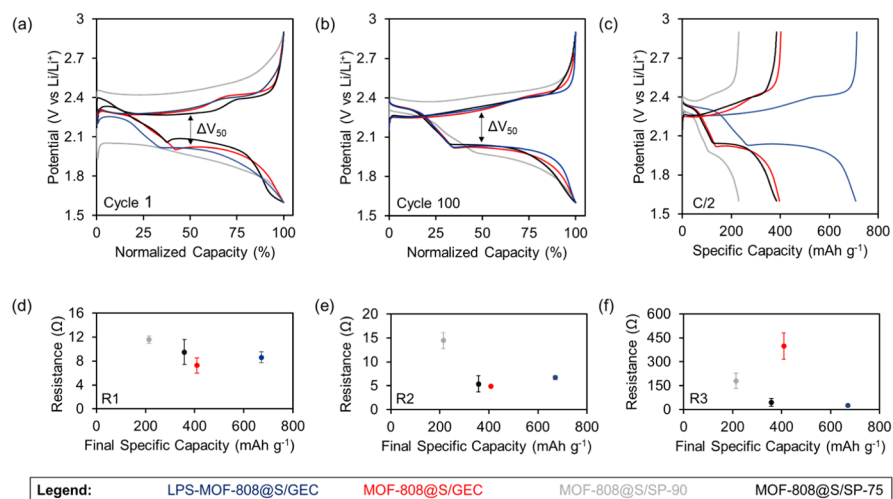


**Figure 5.** Capacity-normalized galvanostatic charge/discharge curves (rate of C/2) for (a) cycle 1 and (b) cycle 100 show differences in electrode polarization, denoted at 50% capacity as  $\Delta V_{50}$ . The un-normalized curves are also provided in (c). Averaged EIS results for (d)  $R_1$ —electrolyte solution resistance, (e)  $R_2$ —electrode surface resistance, and (f)  $R_3$ —charge transfer resistance values are plotted as a function of the capacity after 100 cycles at C/2.

36.6% (Figure S10). The capacity enhancement suggests the functional group has a greater impact on sulfur utilization in the sulfur-loaded MOF compared to MOF physically mixed with sulfur.

We next investigate how the morphologies of the slurry components influence the volumetric performance of these cells. SEM images of MOF-808@S/GEC and LPS-MOF-808@S/GEC cathodes (Figures 4a–c, S11) display more dense slurry coatings compared to MOF-808+S/SP-75 cathodes, with average volumetric loadings calculated in Table S2. From these measurements, it is evident the sulfur-loaded MOF samples exhibit superior packing efficiency on the cathode surface, important for maximizing volumetric output of the cell. We demonstrate this effect in Figure 4d,e, where MOF-808@S/GEC delivers much less capacity per gram of slurry than the conventional MOF-808+S/SP-75 cathode but exhibits comparable performance when examined per cubic centimeter of slurry coating. Similarly, comparing LPS-MOF-808@S/GEC and MOF-808+S/SP-75 cell performances in Figure 4e highlights the significant improvement in volumetric capacity delivery to nearly 900 mA h cm<sup>-3</sup>, achievable using our optimized formulation. We note that our results represent a proof-of-concept as our measurements only account for the slurry thickness and do not include dimensions of the carbon paper current collector. Translation of these slurries to foil current collectors and manipulation of the areal sulfur loading extent would further improve the total volumetric output of the electrode.

Additional electrochemical experiments provide insight into the limitations of the sulfur-loaded MOF cells. In rate capability experiments, increasing C-rate decreases capacity delivered with each incremental step (Figure 4f,g). LPS-MOF-808@S/GEC cells perform well at moderate C-rates, but capacities are markedly decreased as the rate is increased above 2C. This drop in performance at high charge rate is also seen for all of the other cells containing sulfur-loaded MOFs (Figure S12). We attribute this effect to inhibited diffusion inside the sulfur-loaded MOFs, which limits mass transport and thus, the ability to cycle effectively at higher rates. In the MOF-808+S/SP-75 composite, sulfur exists outside the MOF and is less

dependent on mass transport within the cathode at high C-rates than the sulfur-loaded MOF cells (regardless of slurry composition), enabling effective cycling. This hypothesis is confirmed by the nonplateau behavior in the discharge curves of sulfur-loaded MOFs compared to sulfur-mixed MOF cells in Figure S13.<sup>49–51</sup> We further evaluated electrochemically controlled diffusion processes using cyclic voltammetry (Figures S14 and S15, Table S3) and galvanostatic intermittent titration technique (GITT) experiments (Figure S16, Table S4). Both scan-rate dependence cyclic voltammograms and GITT discharge profiles generally show the MOF-808@S/GEC and LPS-MOF-808@S/GEC cells exhibit slower diffusion than the MOF-808+S/SP-75 cell, although significant variations in electrode architecture may also contribute to these results, as discussed more thoroughly in Tables S3 and S4.

The differences in cycling performance prompted us to explore further electrochemical differences among these electrodes. Normalized galvanostatic capacity–voltage curves shown in Figure 5a,b overlap for MOF-808@S/GEC and LPS-MOF-808@S/GEC curves, suggesting their cycling mechanisms and redox equilibration potentials are similar; however, differences arise in the analogous MOF-808@S/SP-90 cell. In particular, significant polarization at a 50% state of discharge (denoted  $\Delta V_{50}$ ) occurs in the MOF-808@S/SP-90 cells in both the first and final cycle at C/2 (Figure 5), indicative of impeded Li<sup>+</sup>/e<sup>-</sup> transport needed for cycling.<sup>52,53</sup> Only when the Super-P/PVDF content is returned to 25% by mass in the slurry formulation, are the voltage differences consistent with the GEC cells. This observed electrode polarization results in diminished energy output of the cell and highlights the deficits of the MOF-808@S/SP-90 cathodes.

Further analysis using electrochemical impedance spectroscopy (EIS) measurements collected from cells after cycling provides insight into electrochemical differences resulting from different slurry compositions (Figure 5e,f). The equivalent circuit used to model impedance data is included with representative Nyquist plots in Figure S17.  $R_1$  is attributed to the electrolyte solution resistance, affected by the dissolution of ionic species that increase the electrolyte

viscosity, predominantly lithium polysulfides. All of the values for sulfur-loaded MOF cells tested are similar to those reported elsewhere.<sup>10,16</sup> Additionally, it is worth noting that GEC-containing cells exhibit lower  $R_1$  values than Super-P/PVDF cells (Figure 5d), supporting the claim that the GEC additive plays a role in the suppression of polysulfide leaching.

$R_2$  is identified as the electrode surface resistance, caused by both deposited sulfur species and electronically isolated islands of the active material. The MOF-808@S/SP-90 cells exhibit three times higher  $R_2$  compared to the MOF-808@S/GEC cells, implying that surface resistance is likely the key contributor to the observed electrode polarization as discussed above. In accordance with our previous discussion, the surface resistance drops when the Super-P/PVDF content is increased to 25% of the slurry mass for MOF-808@S/SP-75.

A similar result is obtained for  $R_3$ , assigned to charge transfer resistance, in which the MOF-808@S/SP-75 cells have lower resistance than the MOF-808@S/SP-90 cells after cycling. The  $R_3$  values are unexpectedly higher for the MOF-808@S/GEC cells compared to MOF-808@S/SP-90 cells despite a smaller electrode polarization. However, introduction of the thiophosphate moiety in LPS-MOF-808@S/GEC lowers the  $R_3$  value, suggesting the charge transfer resistance could be linked to the accessibility of sulfur. This argument is supported by the increased length of the galvanostatic charge/discharge curves (Figure 5c), where the LPS-MOF-808@S/GEC cells utilize more sulfur throughout the discharge process. These results strongly suggest that the thiophosphate improves cyclability by lowering charge transfer resistance, enabling more efficient equilibration along both the upper and lower galvanostatic discharge plateaus.

## CONCLUSIONS

In summary, our graphene nanoflake strategy improves the utility of sulfur-loaded MOF samples for Li–S batteries by improving both the conductivity and interfacial contact in the cathode slurry. The electronic and morphological properties of the GEC additive enable slurry formulations that employ a lower mass of the carbon/binder additive, while also significantly improving the volumetric density of the cathode compared to conventional Super-P/PVDF composites. Extensive physicochemical characterization has been performed on the MOF/GEC nanocomposite electrodes to identify constituent species and investigate interactions between the MOF, sulfur, and carbon/binder components. We further demonstrate that loading sulfur into functionalized MOFs enhances the effect of the functional group, here LPS, resulting in Li–S cells that are able to better access constituent sulfur and deliver higher capacities than the parent MOF/GEC nanocomposite cells. While this work affords additional opportunities for functionalized MOFs in electronic device applications, there is still more to be understood with regard to mass transport limitations in sulfur-loaded versus sulfur-mixed MOF cells. Emerging research may also enable future efforts developing conformal GEC coatings on the MOF particles to enhance electrical conductivity of the cathode and permit scalable processing. Nevertheless, this work presents an exciting materials engineering direction to exploit the diverse chemistry within MOFs and other porous frameworks for advancing energy storage capabilities in electrochemical devices.

## ASSOCIATED CONTENT

### Supporting Information

The Supporting Information is available free of charge at <https://pubs.acs.org/doi/10.1021/acsami.0c09622>.

Experimental section including MOF synthesis, sulfur loading procedure, GEC synthesis, electrochemistry, and instrumentation; TGA results of sulfur-loaded MOF samples; XRD patterns of MOF, sulfur, and sulfur-loaded MOF samples; FT-IR spectra of sulfur-loaded MOF samples; EDS maps of a MOF-808@S particle and the dried MOF-808@S/GEC slurry; TGA results of the GEC sample; size distribution statistics of graphene sheets collected via AFM; description of all slurry formulations; SEM and high-magnification SEM images of dried slurries; Raman spectra; cycling results; cross-sectional SEM images of coated electrodes; measurements used to calculate density of slurry on various cathodes; rate capability experiment results; galvanostatic discharge curves; CV measurements of MOF-containing cells; GITT experiment results; and Nyquist plots (PDF)

## AUTHOR INFORMATION

### Corresponding Authors

**Mark C. Hersam** – Department of Materials Science and Engineering, Department of Chemistry, and Department of Electrical and Computer Engineering, Northwestern University, Evanston, Illinois 60208, United States; [orcid.org/0000-0003-4120-1426](https://orcid.org/0000-0003-4120-1426); Email: [m-hersam@northwestern.edu](mailto:m-hersam@northwestern.edu)

**V. Sara Thoi** – Department of Chemistry and Department of Materials Science and Engineering, Johns Hopkins University, Baltimore, Maryland 21218, United States; [orcid.org/0000-0003-0896-4077](https://orcid.org/0000-0003-0896-4077); Email: [sarathoi@jhu.edu](mailto:sarathoi@jhu.edu)

### Authors

**Avery E. Baumann** – Department of Chemistry, Johns Hopkins University, Baltimore, Maryland 21218, United States;

[orcid.org/0000-0001-8513-8049](https://orcid.org/0000-0001-8513-8049)

**Julia R. Downing** – Department of Materials Science and Engineering, Northwestern University, Evanston, Illinois 60208, United States

**David A. Burns** – Department of Chemistry, Johns Hopkins University, Baltimore, Maryland 21218, United States;

[orcid.org/0000-0002-5067-5511](https://orcid.org/0000-0002-5067-5511)

Complete contact information is available at:

<https://pubs.acs.org/doi/10.1021/acsami.0c09622>

### Author Contributions

#A.E.B. and J.R.D. contributed equally.

### Notes

The authors declare no competing financial interest.

## ACKNOWLEDGMENTS

A.E.B., D.A.B., and V.S.T. thank the National Science Foundation CAREER Award (DMR-1945114) and the Department of Chemistry and Johns Hopkins University (JHU) for instrumentation support, graduate student support, and start-up funding. A.E.B. and D.A.B. also received the Harry and Cleio Greer Fellowships from the JHU Department of Chemistry. A.E.B. acknowledges support from the ARCS Foundation for the Metropolitan Washington Chapter Scholar Award. J.R.D. and M.C.H. thank the National Science

Foundation Scalable Nanomanufacturing Program (NSF CMMI-1727846). J.R.D. also acknowledges the National Consortium for Graduate Degrees for Minorities in Engineering and Science Fellowship sponsored by the 3M Company and Northwestern University. This work made use of the EPIC facility and Keck-II facilities of Northwestern University's NUANCE Center, which has received support from the Soft and Hybrid Nanotechnology Experimental (SHyNE) Resource (NSF ECCS-1542205); the MRSEC program (NSF DMR-1720139) at the Materials Research Center; the International Institute for Nanotechnology (IIN); the Keck Foundation; and the State of Illinois, through the IIN. The MatCI facility at Northwestern University was also used, which is supported by the MRSEC program (NSF DMR-1720139). We also acknowledge Hector Vivanco and Prof. Tyrel McQueen (Dept. of Chemistry, JHU) for XRD instrumentation support, as well as Ethan Secor for initial graphene ink development and consultation, Chen "Leo" Ling for data analysis support, and Jin-Myoung Lim for helpful discussions (Dept. of Materials Science and Engineering, NU).

## REFERENCES

- (1) He, J.; Manthiram, A. A Review on the Status and Challenges of Electrocatalysts in Lithium-Sulfur Batteries. *Energy Storage Mater.* **2019**, *20*, 55–70.
- (2) Chung, S.-H.; Chang, C.-H.; Manthiram, A. Progress on the Critical Parameters for Lithium-Sulfur Batteries to Be Practically Viable. *Adv. Funct. Mater.* **2018**, *28*, 1801188.
- (3) Dong, C.; Gao, W.; Jin, B.; Jiang, Q. Advances in Cathode Materials for High-Performance Lithium-Sulfur Batteries. *iScience* **2018**, *6*, 151–198.
- (4) Tang, H.; Li, W.; Pan, L.; Tu, K.; Du, F.; Qiu, T.; Yang, J.; Cullen, C. P.; McEvoy, N.; Zhang, C. A Robust, Freestanding MXene-Sulfur Conductive Paper for Long-Lifetime Li-S Batteries. *Adv. Funct. Mater.* **2019**, *29*, 1901907.
- (5) Xiao, Z.; Li, Z.; Meng, X.; Wang, R. MXene-Engineered Lithium-Sulfur Batteries. *J. Mater. Chem. A* **2019**, *7*, 22730–22743.
- (6) Jiang, H.; Liu, X.-C.; Wu, Y.; Shu, Y.; Gong, X.; Ke, F.-S.; Deng, H. Metal-Organic Frameworks for High Charge-Discharge Rates in Lithium-Sulfur Batteries. *Angew. Chem., Int. Ed.* **2018**, *57*, 3916–3921.
- (7) Jin, L.; Huang, X.; Zeng, G.; Wu, H.; Morbidelli, M. Conductive Framework of Inverse Opal Structure for Sulfur Cathode in Lithium-Sulfur Batteries. *Sci. Rep.* **2016**, *6*, 32800.
- (8) Zeng, S.; Li, L.; Xie, L.; Zhao, D.; Wang, N.; Chen, S. Conducting Polymers Crosslinked with Sulfur as Cathode Materials for High-Rate, Ultralong-Life Lithium-Sulfur Batteries. *ChemSusChem* **2017**, *10*, 3378–3386.
- (9) Baumann, A. E.; Aversa, G. E.; Roy, A.; Falk, M. L.; Bedford, N. M.; Thoi, V. S. Promoting sulfur adsorption using surface Cu sites in metal-organic frameworks for lithium sulfur batteries. *J. Mater. Chem. A* **2018**, *6*, 4811–4821.
- (10) Baumann, A. E.; Han, X.; Butala, M. M.; Thoi, V. S. Lithium Thiophosphate Functionalized Zirconium MOFs for Li-S Batteries with Enhanced Rate Capabilities. *J. Am. Chem. Soc.* **2019**, *141*, 17891–17899.
- (11) Zheng, J.; Tian, J.; Wu, D.; Gu, M.; Xu, W.; Wang, C.; Gao, F.; Engelhard, M. H.; Zhang, J.-G.; Liu, J.; Xiao, J. Lewis Acid-Base Interactions between Polysulfides and Metal Organic Framework in Lithium Sulfur Batteries. *Nano Lett.* **2014**, *14*, 2345–2352.
- (12) Hong, X.-J.; Tan, T.-X.; Guo, Y.-K.; Tang, X.-Y.; Wang, J.-Y.; Qin, W.; Cai, Y.-P. Confinement of Polysulfides within Bi-Functional Metal-Organic Frameworks for High Performance Lithium-Sulfur Batteries. *Nanoscale* **2018**, *10*, 2774–2780.
- (13) Bai, L.; Chao, D.; Xing, P.; Tou, L. J.; Chen, Z.; Jana, A.; Shen, Z. X.; Zhao, Y. Refined Sulfur Nanoparticles Immobilized in Metal-Organic Polyhedron as Stable Cathodes for Li-S Battery. *ACS Appl. Mater. Interfaces* **2016**, *8*, 14328–14333.
- (14) Park, J. H.; Choi, K. M.; Lee, D. K.; Moon, B. C.; Shin, S. R.; Song, M.-K.; Kang, J. K. Encapsulation of Redox Polysulfides via Chemical Interaction with Nitrogen Atoms in the Organic Linkers of Metal-Organic Framework Nanocrystals. *Sci. Rep.* **2016**, *6*, 25555.
- (15) Mao, Y.; Li, G.; Guo, Y.; Li, Z.; Liang, C.; Peng, X.; Lin, Z. Foldable Interpenetrated Metal-Organic Frameworks/Carbon Nanotubes Thin Film for Lithium-Sulfur Batteries. *Nat. Commun.* **2017**, *8*, 14628.
- (16) Liu, X.; Wang, S.; Wang, A.; Wang, Z.; Chen, J.; Zeng, Q.; Chen, P.; Liu, W.; Li, Z.; Zhang, L. A new cathode material synthesized by a thiol-modified metal-organic framework (MOF) covalently connecting sulfur for superior long-cycling stability in lithium-sulfur batteries. *J. Mater. Chem. A* **2019**, *7*, 24515–24523.
- (17) Xu, G.; Zuo, Y.; Huang, B. Metal-Organic Framework-74-Ni/Carbon Nanotube Composite as Sulfur Host for High Performance Lithium-Sulfur Batteries. *J. Electroanal. Chem.* **2018**, *830–831*, 43–49.
- (18) Zhang, H.; Zhao, W.; Zou, M.; Wang, Y.; Chen, Y.; Xu, L.; Wu, H.; Cao, A. 3D, Mutually Embedded MOF@Carbon Nanotube Hybrid Networks for High-Performance Lithium-Sulfur Batteries. *Adv. Energy Mater.* **2018**, *8*, 1800013.
- (19) Wu, Y.; Jiang, H.; Ke, F. S.; Deng, H. Three-Dimensional Hierarchical Constructs of MOF-on-Reduced Graphene Oxide for Lithium-Sulfur Batteries. *Chem. - Asian J.* **2019**, *14*, 3577–3582.
- (20) Bao, W.; Zhang, Z.; Qu, Y.; Zhou, C.; Wang, X.; Li, J. Confine Sulfur in Mesoporous Metal-Organic Framework @ Reduced Graphene Oxide for Lithium Sulfur Battery. *J. Alloys Compd.* **2014**, *582*, 334–340.
- (21) Zhao, Z.; Wang, S.; Liang, R.; Li, Z.; Shi, Z.; Chen, G. Graphene-Wrapped Chromium-MOF(MIL-101)/Sulfur Composite for Performance Improvement of High-Rate Rechargeable Li-S Batteries. *J. Mater. Chem. A* **2014**, *2*, 13509–13512.
- (22) Pu, Y.; Wu, W.; Liu, J.; Liu, T.; Ding, F.; Zhang, J.; Tang, Z. A Defective MOF Architecture Threaded by Interlaced Carbon Nanotubes for High-Cycling Lithium-Sulfur Batteries. *RSC Adv.* **2018**, *8*, 18604–18612.
- (23) Geng, P.; Cao, S.; Guo, X.; Ding, J.; Zhang, S.; Zheng, M.; Pang, H. Polypyrrole Coated Hollow Metal-Organic Framework Composites for Lithium-Sulfur Batteries. *J. Mater. Chem. A* **2019**, *7*, 19465–19470.
- (24) Zhou, J.; Yu, X.; Fan, X.; Wang, X.; Li, H.; Zhang, Y.; Li, W.; Zheng, J.; Wang, B.; Li, X. The Impact of the Particle Size of a Metal-Organic Framework for Sulfur Storage in Li-S Batteries. *J. Mater. Chem. A* **2015**, *3*, 8272–8275.
- (25) Zhou, J.; Li, R.; Fan, X.; Chen, Y.; Han, R.; Li, W.; Zheng, J.; Wang, B.; Li, X. Rational Design of a Metal-Organic Framework Host for Sulfur Storage in Fast, Long-Cycle Li-S Batteries. *Energy Environ. Sci.* **2014**, *7*, 2715–2724.
- (26) Furukawa, H.; Gándara, F.; Zhang, Y.-B.; Jiang, J.; Queen, W. L.; Hudson, M. R.; Yaghi, O. M. Water Adsorption in Porous Metal-Organic Frameworks and Related Materials. *J. Am. Chem. Soc.* **2014**, *136*, 4369–4381.
- (27) Qi, Q.; Lv, X.; Lv, W.; Yang, Q.-H. Multifunctional Binder Designs for Lithium-Sulfur Batteries. *J. Energy Chem.* **2019**, *39*, 88–100.
- (28) Sun, K.; Cama, C. A.; Huang, J.; Zhang, Q.; Hwang, S.; Su, D.; Marschilok, A. C.; Takeuchi, K. J.; Takeuchi, E. S.; Gan, H. Effect of Carbon and Binder on High Sulfur Loading Electrode for Li-S Battery Technology. *Electrochim. Acta* **2017**, *235*, 399–408.
- (29) Novoselov, K. S.; Fal'ko, V. I.; Colombo, L.; Gellert, P. R.; Schwab, M. G.; Kim, K. A Roadmap for Graphene. *Nature* **2012**, *490*, 192–200.
- (30) Kholmanov, I. N.; Magnuson, C. W.; Aliev, A. E.; Li, H.; Zhang, B.; Suk, J. W.; Zhang, L. L.; Peng, E.; Mousavi, S. H.; Khanikaev, A. B.; Piner, R.; Shvets, G.; Ruoff, R. S. Improved Electrical Conductivity of Graphene Films Integrated with Metal Nanowires. *Nano Lett.* **2012**, *12*, 5679–5683.

- (31) Secor, E. B.; Prabhumirashi, P. L.; Puntambekar, K.; Geier, M. L.; Hersam, M. C. Inkjet Printing of High Conductivity, Flexible Graphene Patterns. *J. Phys. Chem. Lett.* **2013**, *4*, 1347–1351.
- (32) Paton, K. R.; Varrla, E.; Backes, C.; Smith, R. J.; Khan, U.; O'Neill, A.; Boland, C.; Lotya, M.; Istrate, O. M.; King, P.; Higgins, T.; Barwich, S.; May, P.; Puczkarski, P.; Ahmed, I.; Moebius, M.; Pettersson, H.; Long, E.; Coelho, J.; O'Brien, S. E.; McGuire, E. K.; Sanchez, B. M.; Duesberg, G. S.; McEvoy, N.; Pennycook, T. J.; Downing, C.; Crossley, A.; Nicolosi, V.; Coleman, J. N. Scalable Production of Large Quantities of Defect-Free Few-Layer Graphene by Shear Exfoliation in Liquids. *Nat. Mater.* **2014**, *13*, 624–630.
- (33) Liang, Y. T.; Hersam, M. C. Highly Concentrated Graphene Solutions via Polymer Enhanced Solvent Exfoliation and Iterative Solvent Exchange. *J. Am. Chem. Soc.* **2010**, *132*, 17661–17663.
- (34) Chen, K.-S.; Xu, R.; Luu, N. S.; Secor, E. B.; Hamamoto, K.; Li, Q.; Kim, S.; Sangwan, V. K.; Balla, I.; Guiney, L. M.; Seo, J.-W. T.; Yu, X.; Liu, W.; Wu, J.; Wolverson, C.; Dravid, V. P.; Barnett, S. A.; Lu, J.; Amine, K.; Hersam, M. C. Comprehensive Enhancement of Nanostructured Lithium-Ion Battery Cathode Materials via Conformal Graphene Dispersion. *Nano Lett.* **2017**, *17*, 2539–2546.
- (35) Hyun, W. J.; De Moraes, A. C. M.; Lim, J.-M.; Downing, J. R.; Park, K.-Y.; Tan, M. T. Z.; Hersam, M. C. High-Modulus Hexagonal Boron Nitride Nanoplatelet Gel Electrolytes for Solid-State Rechargeable Lithium-Ion Batteries. *ACS Nano* **2019**, *13*, 9664–9672.
- (36) Lin, Z.; Liu, Z.; Fu, W.; Dudney, N. J.; Liang, C. Lithium Polysulfidophosphates: A Family of Lithium-Conducting Sulfur-Rich Compounds for Lithium-Sulfur Batteries. *Angew. Chem., Int. Ed. Engl.* **2013**, *52*, 7460–7463.
- (37) Hyun, W. J.; Chaney, L. E.; Downing, J. R.; de Moraes, A. C. M.; Hersam, M. C. Printable Hexagonal Boron Nitride Ionogels. *Faraday Discuss.* **2020**, DOI: 10.1039/c9fd00113a.
- (38) Palomares, V.; Goñi, A.; Muro, I. G. d.; De Meatza, I.; Bengoechea, M.; Cantero, I.; Rojo, T. Conductive Additive Content Balance in Li-Ion Battery Cathodes: Commercial Carbon Blacks vs. in Situ Carbon from LiFePO<sub>4</sub>/C Composites. *J. Power Sources* **2010**, *195*, 7661–7668.
- (39) Baumann, A. E.; Burns, D. A.; Díaz, J. C.; Thoi, V. S. Lithiated Defect Sites in Zr Metal–Organic Framework for Enhanced Sulfur Utilization in Li–S Batteries. *ACS Appl. Mater. Interfaces* **2019**, *11*, 2159–2167.
- (40) Liu, J.; Zhang, Q.; Sun, Y.-K. Recent Progress of Advanced Binders for Li-S Batteries. *J. Power Sources* **2018**, *396*, 19–32.
- (41) Xu, Z.-L.; Kim, S. J.; Chang, D.; Park, K.-Y.; Dae, K. S.; Dao, K. P.; Yuk, J. M.; Kang, K. Visualization of Regulated Nucleation and Growth of Lithium Sulfides for High Energy Lithium Sulfur Batteries. *Energy Environ. Sci.* **2019**, *12*, 3144–3155.
- (42) Secor, E. B.; Gao, T. Z.; Islam, A. E.; Rao, R.; Wallace, S. G.; Zhu, J.; Putz, K. W.; Maruyama, B.; Hersam, M. C. Enhanced Conductivity, Adhesion, and Environmental Stability of Printed Graphene Inks with Nitrocellulose. *Chem. Mater.* **2017**, *29*, 2332–2340.
- (43) Lin, Z.-J.; Zheng, H.-Q.; Zeng, Y.-N.; Wang, Y.-L.; Chen, J.; Cao, G.-J.; Gu, J.-F.; Chen, B. Effective and Selective Adsorption of Organoarsenic Acids from Water over a Zr-Based Metal–Organic Framework. *Chem. Eng. J.* **2019**, *378*, 122196.
- (44) Zhang, W.; Bu, A.; Ji, Q.; Min, L.; Zhao, S.; Wang, Y.; Chen, J. pKa-Directed Incorporation of Phosphonates into MOF-808 via Ligand Exchange: Stability and Adsorption Properties for Uranium. *ACS Appl. Mater. Interfaces* **2019**, *11*, 33931–33940.
- (45) Dapoz, S.; Betz, N.; Guittet, M.-J.; Le Moël, A. ESCA Characterization of Heparin-like Fluoropolymers Obtained by Functionalization after Grafting Induced by Swift Heavy Ion Irradiation. *Nucl. Instrum. Methods Phys. Res., Sect. B* **1995**, *105*, 120–125.
- (46) Zhu, Y.; Wang, J.; Zhang, F.; Gao, S.; Wang, A.; Fang, W.; Jin, J. Zwitterionic Nanohydrogel Grafted PVDF Membranes with Comprehensive Antifouling Property and Superior Cycle Stability for Oil-in-Water Emulsion Separation. *Adv. Funct. Mater.* **2018**, *28*, 1804121.
- (47) Wang, G.; Sharp, C.; Plonka, A. M.; Wang, Q.; Frenkel, A. I.; Guo, W.; Hill, C.; Smith, C.; Kollar, J.; Troya, D.; Morris, J. R. Mechanism and Kinetics for Reaction of the Chemical Warfare Agent Simulant, DMMP(g), with Zirconium(IV) MOFs: An Ultrahigh-Vacuum and DFT Study. *J. Phys. Chem. C* **2017**, *121*, 11261–11272.
- (48) Wasalathilake, K. C.; Roknuzzaman, M.; Ostrikov, K.; Ayoko, G. A.; Yan, C. Interaction between functionalized graphene and sulfur compounds in a lithium–sulfur battery—a density functional theory investigation. *RSC Adv.* **2018**, *8*, 2271–2279.
- (49) Zhang, T.; Marinescu, M.; Walus, S.; Kovacic, P.; Offer, G. J. What Limits the Rate Capability of Li-S Batteries during Discharge: Charge Transfer or Mass Transfer? *J. Electrochem. Soc.* **2018**, *165*, A6001–A6004.
- (50) Li, L.; Pascal, T. A.; Connell, J. G.; Fan, F. Y.; Meckler, S. M.; Ma, L.; Chiang, Y.-M.; Prendergast, D.; Helms, B. A. Molecular Understanding of Polyelectrolyte Binders That Actively Regulate Ion Transport in Sulfur Cathodes. *Nat. Commun.* **2017**, *8*, 2277.
- (51) Shaibani, M.; Mirshekarloo, M. S.; Singh, R.; Easton, C. D.; Cooray, M. C. D.; Eshraghi, N.; Abendroth, T.; Dörfler, S.; Althues, H.; Kaskel, S.; et al. Expansion-Tolerant Architectures for Stable Cycling of Ultrahigh-Loading Sulfur Cathodes in Lithium-Sulfur Batteries. *Sci. Adv.* **2020**, *6*, No. eaay2757.
- (52) Zhang, J.; Shi, Y.; Ding, Y.; Peng, L.; Zhang, W.; Yu, G. A Conductive Molecular Framework Derived Li<sub>2</sub>S/N,P-Codoped Carbon Cathode for Advanced Lithium–Sulfur Batteries. *Adv. Energy Mater.* **2017**, *7*, 1602876.
- (53) Al Salem, H.; Babu, G.; Rao, C. V.; Arava, L. M. R. Electrocatalytic Polysulfide Traps for Controlling Redox Shuttle Process of Li-S Batteries. *J. Am. Chem. Soc.* **2015**, *137*, 11542–11545.